PHYSICAL REVIEW B VOLUME 1, NUMBER 12 15 JUNE 1970

Reflection Studies of Coupled Magnetoplasma-Phonon Modes

Richard W. Stimets* and Benjamin Lax†

Francis Bitter National Magnet Laboratory,‡ Massachusetts Institute of Technology, Cambridge, Massachusetts 02139

(Received 6 October 1969)

Far-infrared reflectivity spectra of doped polar semiconductors such as InAs and GaSb exhibit dispersion anomalies which are associated with coupled optical-phonon and plasmon modes and are strongly influenced by magnetic fields. This work examines the behavior of the coupled magnetoplasma–optical-phonon modes as a function of magnetic field. The experimental reflectivity curves, obtained by Fourier transform spectroscopy, are analyzed by means of the Kramers-Kronig relations to obtain the complex dielectric function ϵ. The frequencies and linewidths of the singularities and zeros of ϵ are obtained from the peaks in the curves of $\mathrm{Im}(\epsilon)$ and $\mathrm{Im}(1/\epsilon)$, respectively, and plotted as a function of magnetic field. Using classical equations of motion for lattice ions and conduction electrons, including phenomenological scattering frequencies for both the lattice and the electrons, expressions for the frequencies and effective linewidths of the modes are developed. Theoretical curves of frequency and linewidth versus magnetic field are computed and compared with experiment. Good agreement between theory and experiment is obtained.

I. INTRODUCTION

In a doped polar semiconductor, which consists of a lattice of positive and negative ions together with a plasma of free carriers, there is a coupling between the optical lattice vibrations and plasma oscillations. The coupling occurs through the macroscopic electric field produced when either the lattice ions or free carriers are displaced from equilibrium. The normal modes of the system are mixtures of lattice modes (phonons) and plasma modes (plasmons). As the plasma frequency ω_p increases relative to the longitudinal optical (LO) phonon frequency ω_l the normal mode frequencies do not cross but repel each other as the normal modes exchange roles. The mixing and mode repulsion become significant when ω_p is comparable with ω_l. In n-type III–V compounds this occurs when the electron concentration is in the neighborhood of 10^{17} cm^{-3}.

When an external dc magnetic field is applied to the semiconductor the effect on the lattice modes is negligible because of the large mass of the lattice ions. The free carriers are much lighter and the normal modes of the magnetoplasma depend on magnetic field. Because of the plasma–optical-phonon coupling the normal modes of the magnetoplasma–optical-phonon system are, in general, field dependent. Strong mixing and mode repulsion occur when the free carrier cyclotron frequency ω_c is comparable with ω_l.

The subject of plasma–optical-phonon coupling has been treated theoretically by a number of workers.[1-6] Considering the system classically in the long-wavelength limit, Yokota[1] obtained two coupled equations of motion and derived the equation for the frequencies of the two longitudinal normal modes. Varga[2] showed that the assumption made in the classical treatment that the polarizabilities of the lattice and plasma are additive is justified on the basis of self-consistent field theory. He obtained the total dielectric function and equated it to zero to get the longitudinal mode frequencies. In addition, he considered the behavior of the coupled modes as a function of wave vector k in the region where k is comparable with k_F, the Fermi wave vector of the plasma. Singwi and Tosi[3] considered the coupling from a quantum mechanical point of view. Starting with the electron-phonon Hamiltonian valid in the long-wavelength limit, they arrived at the same equation for the longitudinal normal mode frequencies obtained from the classical theory.

Yokota[4] also considered the classical theory of magnetoplasma–optical-phonon coupling. He obtained the expressions for the long-wavelength dielectric function in both the Faraday and Voigt configurations and noted the occurrence of two additional singularities in the Voigt configuration. Greene, Houghton, and Quinn[5] derived the general expression for the dielectric function when the propagation is at an arbitrary direction to the magnetic field. Rabitz and Lax[6] have recently developed a many-body treatment of the coupled magnetoplasma–optical-phonon system which yields both the singularities and zeros of ϵ.

Three basic techniques have been used to study the coupled modes: (a) optical experiments using both transmission and reflection, (b) Raman scattering, and (c) inelastic neutron scattering. In

normal-incidence transmission experiments, resonance peaks in the absorption are observed at the singularities of the dielectric function. The plasma–optical-phonon system shows a single absorption peak at the transverse optic (TO) phonon frequency ω_t. The longitudinal coupled modes do not interact with electromagnetic (EM) radiation and are therefore unobservable. However, the longitudinal modes can be excited by EM radiation at oblique incidence with the electric vector $\vec{E}$ polarized in the plane of incidence, in which case $\vec{E}$ in the sample has a longitudinal component. Using this technique the Naval Research Laboratory-University of Pennsylvania (NRL – U. of Penn.) group[7] observed an absorption peak in a thin specimen of n-type GaAs which they interpreted as being due to the higher-frequency longitudinal coupled plasmonlike mode. The lower-frequency phononlike mode could not be observed due to strong absorption by both the TO phonon and free carriers.

In the Voigt configuration, the coupled magnetoplasma–optical-phonon modes are partly transverse in nature and interact with EM radiation. Two additional singularities of ϵ are observed as resonance absorption peaks in addition to the peak due to the TO phonon. The NRL – U. of Penn. group[8] observed the coupled magnetoplasma–optical-phonon modes in thin samples of n-type InSb. The experimental dependence of the coupled mode frequencies on magnetic field was found to be in good agreement with classical theory. The qualitative dependence of linewidth and intensity on field was also good although a quantitative study was not carried out. The lower-frequency mode could not be observed in any of the samples when its frequency was between ω_t and ω_l due to the low strength of its absorption line and the presence of strong TO phonon absorption in this region.

Mooradian and Wright[9] used a 1.06-μ YAlG laser to observe the coupled plasma optical phonon by Raman scattering in n-type GaAs. As a function of ω_p the frequencies were found to be in good agreement with the theory but the linewidth and intensity dependence could not be studied carefully due to sample inhomogeneities.

Inelastic neutron scattering is the only technique by which large enough momentum transfer may be achieved to observe the modes in the region $k \approx k_F$ in which the plasma dispersion is significant. Cowley and Dolling[10] were able to observe the effect of plasma–optical-phonon coupling in a study of coherent one-phonon scattering of slow neutrons from n-type single-crystal PbTe. Measuring the dispersion of the LO phonon mode they found a marked decrease in frequency at $k \approx k_F$ for $k \to 0$ due to the interaction with the plasma.

Recently, Bishop[11] has reported the observation of the coupled modes in Voigt transmission experiments in n-type PbTe, in which the constant energy surfaces are highly anisotropic. Bishop and Henvis[12] have achieved better results using reflection measurements and have found good agreement between the experimental reflection spectra and the theory of Wallace.[13,14]

The present work was motivated by several considerations: First, reflection experiments on the coupled modes had not been done before this work.[15,16] Reflection had been used successfully in the study of magnetoplasma effects.[17] The reflection technique has the advantage over the transmission method that the properties of the zeros of the dielectric function may be studied in addition to the singularities. Using the Kramers-Kronig relations the experimental dielectric function may be calculated from the reflectivity curve and compared directly with the theoretical one. Second, the lower frequency had not been observed by transmission in the reststrahl region between ω_t and ω_l. It was hoped that by using reflection the difficulties encountered in transmission might be overcome and the mode could be seen in this region. Third, it was desired to have a really quantitative study of linewidths. The linewidths indicate clearly the changing character of the modes with magnetic field.

The work concentrated on n-type InAs because the coupled modes in this material had not been studied and because the electron effective mass is such that the region of strong mixing lay in the middle of the range of available magnetic field. Some experiments were also carried out with n-type GaSb but, owing to the heavier electron mass, the permissible tuning of the cyclotron frequency was not as great.

II. THEORY

In a doped polar semiconductor, there are three components which contribute to the long-wavelength optical response: the lattice ions, the free carrier plasma, and the interband electron transitions. For optical waves with frequencies in the far infrared, the magnitude of the associated wave propagation vector $\vec{k}$ is of the order of 10^4 cm^{-1} which is small compared to both the Brillouin-zone edge ($\approx 10^8$ cm^{-1}) and the Fermi wave vector of the plasma ($\approx 10^6$ cm^{-1}). Thus, the dispersion of both the optical lattice modes and the longitudinal plasma mode may be neglected and a constant frequency assumed for each. Photon energies in the far infrared are well below all energy gaps (e.g., for InAs $\hbar\omega_t = 0.0275$ eV, for the lowest

gap $\mathcal{E}_g = 0.41$ eV), so that the interband electron transitions contribute simply a constant dielectric susceptibility χ_∞. The optical modes of the system may be described by the classical equations of motion for lattice ions and electrons combined with the equations of classical electrodynamics. The dispersion of the modes arises from the interaction of the coupled lattice and plasma modes with EM radiation.

Let us treat specifically the case of an isotropic polar semiconductor in the presence of a magnetic field, which is taken to be along the z-axis. Our treatment follows that of Born and Huang,[18] with the inclusion of the magnetoplasma. The direct effect of the magnetic field on the lattice ions is negligible because of their large mass. The equations of motion for the lattice ions and the conduction electrons, the polarization equation, Maxwell's equations, and the constitutive relation are, respectively, as follows:

$$\ddot{\vec{u}} + \omega_t^2 \vec{u} + \gamma_t \dot{\vec{u}} = (e^*/M)\vec{E} \quad , \tag{1}$$

$$\ddot{\vec{r}} + \omega_c(\dot{\vec{r}} \times \hat{i}_z) + \gamma_e \dot{\vec{r}} = -(e/m^*)\vec{E} \quad , \tag{2}$$

$$\vec{P} = Ne^*\vec{u} - ne\vec{r} + \chi_\infty \vec{E} \quad , \tag{3}$$

$$\nabla \cdot \vec{H} = 0 \quad , \tag{4}$$

$$\nabla \cdot \vec{D} = 0 \quad , \tag{5}$$

$$\nabla \times \vec{H} = (1/c)\dot{\vec{D}} \quad , \tag{6}$$

$$\nabla \times \vec{E} = -(1/c)\dot{\vec{H}} \quad , \tag{7}$$

$$\vec{D} = \vec{\epsilon} \cdot \vec{E} = \vec{E} + 4\pi \vec{P} \quad . \tag{8}$$

Here $\vec{u} = \vec{u}_+ - \vec{u}_-$ is the relative displacement of the positive and negative ions, e^* their effective charge, and M their reduced mass; $\vec{r}$ is the average displacement of the electrons and m^* their effective mass; ω_t is the transverse-optical-phonon frequency, ω_c the cyclotron frequency, and γ_t and γ_e are scattering frequencies for the lattice and plasma; N and n are the lattice-ion and electron densities, respectively.

The fields in the above equations are all macroscopic, i.e., averaged over a unit cell of the crystal. In this regard, some care must be taken in the interpretation of Eq. (1). The lattice ions actually respond to the local field $\vec{E}_{\text{loc}}$, which for lattices of tetrahedral symmetry is related to the macroscopic field by $\vec{E}_{\text{loc}} = \vec{E} + \frac{4}{3}\pi\vec{P}$, the second term being the Lorenz field correction. In Eq. (1), the microscopic equations of motion for both positive and negative ions have been combined in such a way as to separate the local and macroscopic forces. The local or elastic restoring force, embodied in the second term, includes both the force from the overlap potential of the ions and that due to the Lorenz field.[19] The macroscopic force is represented in Eq. (1) by $\vec{E}$ and gives rise to the difference between the TO and LO phonon frequencies. $\vec{E}$ is the total internal macroscopic electric field, and when the medium is driven by an external field as in an optical experiment, $\vec{E}$ includes both the external field and the polarization field produced internally.

As Varga has shown,[2] the presence of conduction electrons does not alter the validity of Eq. (1). The screening length of the electrons is large compared to a lattice constant. Hence the electrons respond to and contribute to only the macroscopic field $\vec{E}$, and there is no additional local field correction for the lattice ions. As a consequence, the susceptibilities of the lattice and the plasma may be simply added, and the polarization is a sum of terms from the lattice, plasma, and interband electron transitions.

The lattice and the plasma are coupled through the internal macroscopic electric field. Displacement of either component polarizes the medium, producing an electric field which acts on the other component.

The lattice scattering frequency γ_t takes into account phenomenologically the loss of optical phonons through multiphonon interactions. In general, several mechanisms may be responsible for the plasma loss, which is accounted for by the plasma scattering frequency γ_e. However, at low temperatures and optical wavelengths this loss arises almost entirely from single-particle scattering by impurity ions. Collective loss mechanisms such as Landau damping become important only at much larger values of k.

For a plane wave of the form $e^{i(\vec{k}\cdot\vec{x} - \omega t)}$, the equations of motion combined with the polarization equation and the constitutive relation yield the dielectric tensor $\vec{\epsilon}$ whose components are

$$\epsilon_{xx} = \epsilon_\infty \left(\frac{\omega^2 - \omega_l^2 + i\omega\gamma_t}{\omega^2 - \omega_t^2 + i\omega\gamma_t} - \frac{\omega_p^2(\omega^2 + i\omega\gamma_e)}{(\omega^2 + i\omega\gamma_e)^2 - \omega^2\omega_c^2} \right), \tag{9}$$

$$\epsilon_{xy} = -\epsilon_{yx} = \epsilon_\infty \{ i\omega_p^2 \omega\omega_c / [(\omega^2 + i\omega\gamma_e)^2 - \omega^2\omega_c^2] \}, \tag{10}$$

$$\epsilon_{zz} = \epsilon_\infty \left(\frac{\omega^2 - \omega_l^2 + i\omega\gamma_t}{\omega^2 - \omega_t^2 + i\omega\gamma_t} - \frac{\omega_p^2}{(\omega^2 + i\omega\gamma_e)} \right), \tag{11}$$

where $\epsilon_\infty = 1 + 4\pi\chi_\infty$, the high-frequency dielectric constant; $\omega_p = (4\pi ne^2/m^*\epsilon_\infty)^{1/2}$, the electron plasma frequency; and

$$\omega_l = [\omega_t^2 + (4\pi Ne^{*2}/M\epsilon_\infty)]^{1/2},$$

the LO phonon frequency.

Maxwell's equations yield the following two equations which describe, respectively, the behavior of the longitudinal and transverse components of the electric field:

$$\vec{k}\cdot\vec{\epsilon}\,\vec{E}=0 \quad , \tag{12}$$

$$\vec{k}\times\vec{k}\times\vec{E}+(\omega^2/c^2)\,\vec{\epsilon}\,\vec{E}=0. \tag{13}$$

With no external magnetic field or in the Faraday configuration the normal modes resolve into purely longitudinal and transverse types. In both cases, Eq. (12) yields the longitudinal mode frequencies, which are independent of $\vec{k}$, while Eq. (13) results in the dispersion relation for the transverse modes:

$$k^2=(\omega^2/c^2)\epsilon \quad , \tag{14}$$

where ϵ is the effective dielectric function. For all other directions of propagation all of the modes are at least partly transverse in nature, and Eqs. (12) and (13) together yield dispersion relations of the form of Eq. (14).

We shall consider the normal modes in detail in three special cases: (i) $H=0$. In this case $\vec{\epsilon}$ becomes a scalar dielectric function $\epsilon(0)$. $\epsilon(0)$ is the effective dielectric function for the transverse modes. The longitudinal mode frequencies are given by

$$\epsilon(0)=0 \quad . \tag{15}$$

(ii) Faraday configuration ($\vec{k}\parallel\vec{H}$). The transverse and longitudinal modes are separate because the longitudinal electron motion is along the magnetic field and unaffected by it. The equation for the longitudinal mode frequencies is

$$\epsilon_{zz}=0 \quad , \tag{16}$$

which is the same as $H=0$. The effective dielectric functions for the right and left circularly polarized modes, respectively, are

$$\epsilon_{\pm}=\epsilon_{xx}\pm i\epsilon_{xy} \quad . \tag{17}$$

(iii) Voigt configuration ($\vec{k}\perp\vec{H}$). Due to the presence of the magnetic deflecting force on the electrons, the modes do not separate into longitudinal and transverse types but into modes with the electric vector perpendicular to and parallel to $\vec{H}$. The effective dielectric functions are, respectively,

$$\epsilon_{\perp}=\epsilon_{xx}+(\epsilon_{xy}^2/\epsilon_{xx})=2\epsilon_{+}\epsilon_{-}/(\epsilon_{+}+\epsilon_{-}) \quad , \tag{18}$$

$$\epsilon_{\parallel}=\epsilon_{zz} \quad . \tag{19}$$

Let us now study the behavior of the modes when losses are neglected. In this case the algebra simplifies considerably and we may more easily obtain a qualitative understanding of the nature of the modes and their effect on the optical properties of the material. Also, if losses are small, the corrections to the normal mode frequencies are of second order so that the lossless solutions for the mode frequencies are a good approximation even when loss is included.

If $\gamma_t=\gamma_e=0$, we have

$$\epsilon(0)=\epsilon_{\infty}[(\omega^2-\omega_l^2)/(\omega^2-\omega_t^2)-(\omega_p^2/\omega^2)], \tag{20}$$

$$\epsilon_{\pm}=\epsilon_{\infty}\{(\omega^2-\omega_l^2)/(\omega^2-\omega_t^2)-[\omega_p^2/\omega(\omega\mp\omega_c)]\}. \tag{21}$$

$\epsilon(0)$ has three anomalies – one singularity at ω_t and two zeros at the two positive roots of the equation

$$\omega^4-(\omega_p^2+\omega_l^2)+\omega_p^2\omega_t^2=0 \quad . \tag{22}$$

We shall refer to the lower and upper frequencies as ω_A and ω_B, respectively. ϵ_{+} has a singularity at ω_t and one at ω_c where pure cyclotron resonance occurs: ϵ_{-} has only one singularity at ω_t. ϵ_{+} and ϵ_{-} each have two zeros given, respectively, by the roots of the two quartic equations

$$\omega^4\mp\omega_c\omega^3-(\omega_l^2+\omega_p^2)\,\omega^2\pm\omega_c\omega_l^2\omega+\omega_p^2\omega_t^2=0 \quad . \tag{23}$$

Each of these equations has two positive and two negative roots, and the roots of one are the negatives of the roots of the other as can be seen by changing the sign of ω throughout. (Changing the sign of ω is equivalent to changing the direction of $\vec{k}$ which simply reverses the sense of polarization.) Let us designate the four positive roots in order of increasing frequency as ω_1, ω_2, ω_3, and ω_4, respectively. $\epsilon_{\perp}$ has a singularity at ω_t and two additional singularities given by the two positive roots of the equation

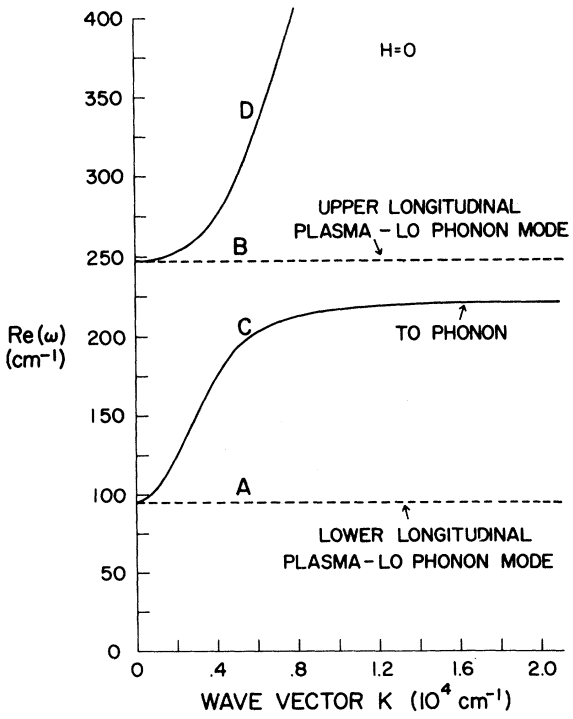

FIG. 1. Dispersion of the coupled plasma–optical–phonon modes.

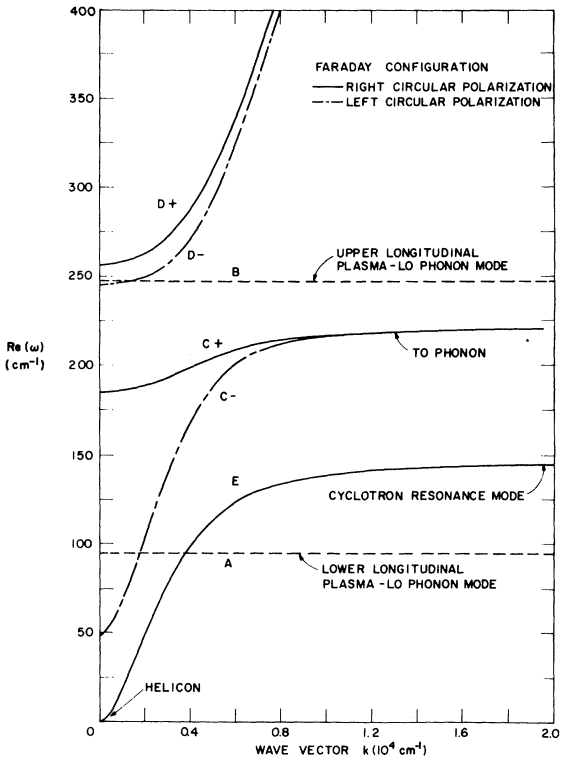

FIG. 2. Dispersion of the coupled magnetoplasma–optical-phonon modes in the Faraday configuration. (H = 39.5 kG.)

$$\omega_4 - (\omega_p^2 + \omega_l^2 + \omega_c^2)\omega^2 + \omega_l^2\omega_c^2 + \omega_p^2\omega_t^2 = 0 \quad . \qquad (24)$$

The lower and upper frequencies will be termed ω_a and ω_b, respectively. As can be seen from Eq. (18), the zeros of $\epsilon_\perp$ are the zeros of ϵ_+ and ϵ_-. This is evident because at $\epsilon = 0$, i.e., $k = 0$, there is no distinction between the Faraday and Voigt configurations.

The dispersion of the normal modes is shown in Figs. 1–3. The purely longitudinal modes do not interact with EM radiation and they show no dispersion. The transverse modes are partly radiative and therefore are dispersive and exhibit mode repulsion as a function of k. In the regions of frequency in which the effective dielectric functions are negative the transverse modes are attenuated and do not propagate. The zeros and singularities of the dielectric function correspond to the anomalies in the propagation of the transverse modes, i.e., $k \to 0$ and $k \to \infty$ (i.e., $k \gg \omega/c$ but small compared to the Brillouin-zone edge and the Fermi wave vector), respectively.

For $H = 0$ (Fig. 1) the longitudinal modes A and B occur at frequencies ω_A and ω_B, respectively. Because of the plasma–optical-phonon interaction they are mixed modes having both lattice and plasma content. For the particular parameters chosen here, A is mainly plasmonlike and B mainly phononlike. Transverse modes C and D become identical in character with their longitudinal counterparts for $k \to 0$. As $k \to \infty$ the lattice, plasma, and EM radiation field all become independent. Mode C becomes a pure TO phonon while D becomes a pure photon.

In the Faraday configuration (Fig. 2), the longitudinal modes are unaffected by the magnetic field. For $k \to 0$ transverse modes C_+, C_-, D_+, and D_- all have both lattice and plasma content. In contrast to the $H = 0$ situation, they do not become identical with the longitudinal modes as $k \to 0$ because the medium is now anisotropic due to the magnetic field. As $k \to \infty$, C_+ and C_- both become a pure TO phonon while D_+ and D_- both become a pure photon. Transverse mode E is a helicon with the dispersion relation

$$\omega = (c^2\omega_c k^2/\epsilon_\infty \omega_p^2)$$

at small k. As $k \to \infty$ it becomes a pure cyclotron resonance mode with frequency ω_c.

In the Voigt configuration (Fig. 3) modes A and B are no longer purely longitudinal but are partly transverse in character so that they show dispersion. For $k \to 0$ modes A, B, C, and D are identical with modes C_-, D_-, C_+, and D_+, respectively, in the Faraday configuration. As $k \to \infty$ C becomes

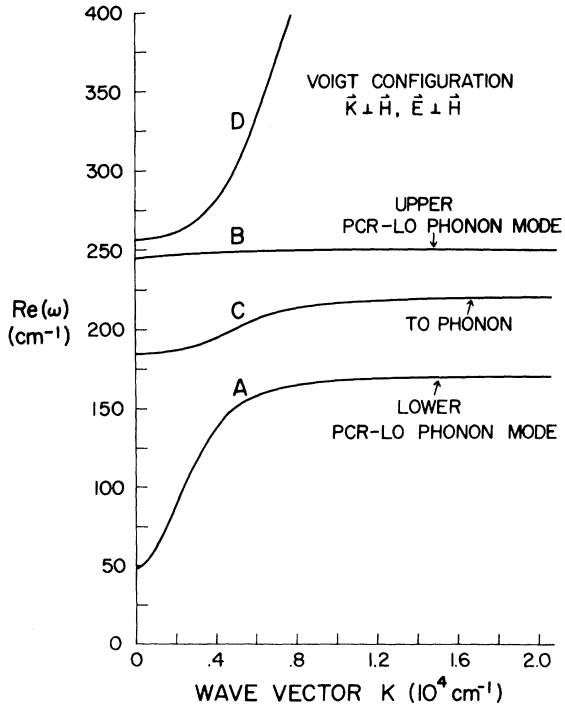

FIG. 3. Dispersion of the coupled magnetoplasma–optical-phonon modes in the Voigt configuration. (H = 39.5 kG.)

a TO phonon and D a photon as before. A and B become plasma-cyclotron resonance LO phonon (PCR LO phonon) modes which involve only longitudinal lattice motion but both longitudinal and transverse plasma motion.

In order to gain a better physical understanding of the modes let us consider the forces involved. The lattice ions respond to the elastic restoring force and the macroscopic electric field; the electrons respond to the electric field only. From Eqs. (8), (12), and (13) we obtain the longitudinal and transverse components of the electric field in terms of the polarization:

$$E_l = -4\pi P_l \quad , \tag{25}$$

$$E_t = -4\pi P_t/[1-(c^2k^2/\omega^2)] \quad . \tag{26}$$

For longitudinal vibrations the relation between E and P is independent of k. The electric force adds to the elastic restoring force so that the frequency is greater than that resulting from the elastic force alone. For transverse vibrations the relation between E and P is the same as in the longitudinal case for $k \to 0$. For $k \to \infty$ the ratio of E to P tends to zero and the electric force becomes negligible. In this case the electric force subtracts from the elastic restoring force so that the frequency approaches the frequency of elastic vibration from below. The electric fields in Eqs. (25) and (26) are qualitatively different. The longitudinal electric field is purely electrostatic; the $\nabla \cdot \vec{H} = 0$ condition dictates that the associated time-varying magnetic field must vanish. The transverse electric field, on the other hand, is electromagnetic, having an associated time-varying magnetic field $H_t = (ck/\omega)E_t$.

The reflectivity for normally incident EM radiation is given in terms of the effective dielectric function by

$$R = \left| (\epsilon^{1/2}-1)/(\epsilon^{1/2}+1) \right|^2 . \tag{27}$$

From Eq. (27), it is evident that in the frequency regions where ϵ is negative and the modes do not propagate, $R = 1$, i.e., there is perfect reflection. The anomalies of the dielectric function appear as edges in the reflectivity curve. As ϵ goes through a singularity, R rises steeply and stays at unity in the region of negative ϵ. As ϵ goes through zero and becomes positive again, R falls abruptly to zero where $\epsilon = 1$ and then rises as ϵ increases. Thus the falling and rising edges of the reflectivity spectrum correspond, respectively, to the zeros and singularities of the dielectric function and to the $k \to 0$ and $k \to \infty$ dispersion anomalies.

From the foregoing discussion, the qualitative features of the reflectivity spectrum for the magmetoplasma–optical-phonon system can be understood by a consideration of the lossless case. For $H = 0$ falling edges occur at ω_A and ω_B and a rising edge at ω_t. In the Faraday configuration for right circular polarization, R has falling edges at ω_3 and ω_4 and rising edges at ω_c and ω_t; for left circular polarization there are falling edges at ω_1 and ω_2 and a rising edge at ω_t. In the Voigt configuration, R has falling edges at ω_1, ω_2, ω_3, and ω_4 and rising edges at ω_a, ω_b, and ω_t. Thus, in the Voigt configuration all of the dielectric anomalies except pure cyclotron resonance are manifest in the reflectivity spectrum.

In the lossless case, the effective dielectric function may be written as a quotient in which both the numerator and denominator are products of factors of the form $(\omega^2 - \omega_i^2)$, where the ω_i are the frequencies of the anomalies. For the Faraday configuration, ϵ_+ and ϵ_- cannot be written in this way but the product $\epsilon_+\epsilon_-$ which contains the anomalies of both ϵ_+ and ϵ_- can. When losses are included a similar procedure may be followed using factors of the form $(\omega^2 - \omega_i^2 + i\omega\gamma_i)$ where the γ_i are effective scattering frequencies. By comparison with the original expressions for the dielectric functions [Eqs. (9)–(11), (17), and (18)] we obtain a set of coupled equations for the ω_i and γ_i in terms of ω_t, ω_l, ω_p, ω_c, γ_t, and γ_e. Considerable simplification results if we make the physically realistic assumption that the loss is small, i.e., γ_t, $\gamma_e \ll \omega$, ω_t, ω_l, ω_p. Then, terms involving products of the scattering frequencies are of second order and may be neglected. As a consequence, the ω_i are the same as in the lossless case, while the γ_i are given by a set of simultaneous equations.

In the small-loss approximation, the effective dielectric functions may be written

$$\epsilon(0) = \frac{(\omega^2 - \omega_A^2 + i\omega\gamma_A)(\omega^2 - \omega_B^2 + i\omega\gamma_B)}{(\omega^2 + i\omega\gamma_e)(\omega^2 - \omega_t^2 + i\omega\gamma_t)} \quad , \tag{28}$$

$$\epsilon_+\epsilon_- = \frac{(\omega^2 - \omega_1^2 + i\omega\gamma_1)(\omega^2 - \omega_2^2 + i\omega\gamma_2)(\omega^2 - \omega_3^2 + i\omega\gamma_3)(\omega^2 - \omega_4^2 + i\omega\gamma_4)}{\omega^2(\omega^2 - \omega_t^2 + i\omega\gamma_t)^2(\omega^2 - \omega_c^2 + 2i\omega\gamma_e)} \quad , \tag{29}$$

$$\epsilon_\perp = \frac{(\omega^2 - \omega_1^2 + i\omega\gamma_1)(\omega^2 - \omega_2^2 + i\omega\gamma_2)(\omega^2 - \omega_3^2 + i\omega\gamma_3)(\omega^2 - \omega_4^2 + i\omega\gamma_4)}{(\omega^2 + i\omega\gamma_o)(\omega^2 - \omega_t^2 + i\omega\gamma_t)(\omega^2 - \omega_a^2 + i\omega\gamma_a)\quad(\omega^2 - \omega_b^2 + i\omega\gamma_b)} \quad . \tag{30}$$

γ_A and γ_B are given by the two simultaneous equations

$$\gamma_A+\gamma_B=\gamma_e+\gamma_t \quad , \tag{31}$$

$$\omega_B^2\gamma_A+\omega_A^2\gamma_B=\omega_l^2\gamma_e+\omega_p^2\gamma_t \quad , \tag{32}$$

while γ_1, γ_2, γ_3, and γ_4 are solutions of the four simultaneous equations

$$\sum_i^4\gamma_i=2\gamma_t+2\gamma_e \quad , \tag{33}$$

$$\sum_{i\neq j}^4\omega_j^2\gamma_i=2(\omega_l^2+\omega_c^2+2\omega_p^2)\gamma_t+2(2\omega_l^2+\omega_p^2)\gamma_e \quad , \tag{34}$$

$$\sum_{i\neq j\neq k}^4\omega_k^2\omega_j^2\gamma_i=2(\omega_l^2\omega_c^2+\omega_p^2\omega_l^2+\omega_p^2\omega_t^2+\omega_p^4)\gamma_t + 2(\omega_l^4+\omega_p^2\omega_l^2+\omega_p^2\omega_t^2)\gamma_e \quad , \tag{35}$$

$$\sum_{i\neq j\neq k\neq m}\omega_m^2\omega_k^2\omega_j^2\gamma_i=2\omega_p^4\omega_t^2\gamma_t+2\omega_p^2\omega_l^2\omega_t^2\gamma_e \quad , \tag{36}$$

and γ_a, γ_b, and γ_o are given by the three simultaneous equations

$$\gamma_a+\gamma_b+\gamma_o=\gamma_t+2\gamma_e \quad , \tag{37}$$

$$\omega_b^2\gamma_a+\omega_a^2\gamma_b+(\omega_a^2+\omega_b^2)\gamma_o=(\omega_c^2+\omega_p^2)\gamma_t+(2\omega_c^2+\omega_p^2)\gamma_e \quad , \tag{38}$$

$$\omega_a^2\omega_b^2\gamma_o=\omega_p^2\omega_t^2\gamma_e \quad . \tag{39}$$

When losses are present, the normal mode frequencies have imaginary parts, i.e., they posses finite lifetimes. For the longitudinal modes and the transverse modes in the limits $k\to 0$ and $k\to\infty$ there is a simple relation between the imaginary part of the frequency and the effective scattering frequency. The normal mode frequencies are given by equations of the form

$$\omega^2-\omega_i^2+i\omega\gamma_i=0 \quad , \tag{40}$$

which has the solutions in the small-loss approximation

$$\mathrm{Re}(\omega)=\omega_i \quad , \tag{41}$$

$$\mathrm{Im}(\omega)=-\tfrac{1}{2}\gamma_i \quad . \tag{42}$$

For the transverse modes at arbitrary k, $\mathrm{Im}(\omega)$ is a function of k. The frequencies ω_i and effective scattering frequencies γ_i of the transverse modes in the limits $k\to 0$ and $k\to\infty$ are determined directly from an optical measurement of the dielectric function. The singularities of ϵ appear as resonances in $\mathrm{Im}(\epsilon)$. If the resonances are well separated, we have near a particular resonance

$$\mathrm{Im}(\epsilon)\sim\omega\gamma_i C/[(\omega-\omega_i)^2+\omega^2\gamma_i^2] \quad , \tag{43}$$

where C is a slowly varying function of ω. In the small-loss approximation the maximum occurs at ω_i and the linewidth, i.e., the full width at half-maximum is γ_i. In an identical fashion the zeros of ϵ appear as resonances in $\mathrm{Im}(1/\epsilon)$.

The effective scattering frequencies can best be understood by considering the energy density of the modes. Extending the expression given by Born and Huang[19] to include the plasma, we obtain for the energy density

$$\mathcal{E}=\tfrac{1}{2}NM\dot{u}^2+\tfrac{1}{2}nm^*\dot{r}^2+\tfrac{1}{2}NM\omega_t^2u^2+(1/8\pi)(\epsilon_\infty E^2+H_t^2) \quad . \tag{44}$$

The first three terms are, respectively, the lattice kinetic, plasma kinetic, and lattice potential energy densities. The fourth term represents electrostatic energy for the longitudinal modes and electromagnetic energy for the transverse modes. H_t is the transverse time-varying magnetic field. For $k\to 0$, $H_t\to 0$. For $k\to\infty$, the electromagnetic energy density becomes vanishingly small; the energy of the transverse modes becomes entirely mechanical in nature.

As determined above, the modes are damped as $e^{-(\gamma/2)t}$. Since $\mathcal{E}$ involves the square of the coordinates, it is damped as $e^{-\gamma t}$. Thus, the physical meaning of the effective scattering frequency γ is

$$\gamma=\frac{\text{average power loss per unit volume}}{\text{total energy density}}=\frac{\overline{P}}{\mathcal{E}} \quad . \tag{45}$$

The total power loss is given by

$$P=NM\gamma_t\dot{\vec{u}}\cdot\dot{\vec{u}}+nm^*\gamma_e\dot{\vec{r}}\cdot\dot{\vec{r}} \quad , \tag{46}$$

so that γ may be written in terms of the time average of lattice kinetic, plasma kinetic, and potential energy densities, $\overline{T}_L$, $\overline{T}_p$, and $\overline{V}$, respectively, as

$$\gamma=(2\gamma_t\overline{T}_L+2\gamma_e\overline{T}_p)/(\overline{T}_L+\overline{T}_p+\overline{V}) \quad . \tag{47}$$

When $H_t=0$, the average kinetic and potential energy densities are equal, i.e., $T=\overline{V}$. (The electromagnetic energy of the transverse modes is included in $\overline{V}$.) The energy oscillates back and forth between kinetic and potential forms. In this case γ may be written as

$$\gamma=f\gamma_t+(1-f)\gamma_e \quad , \tag{48}$$

where $f=\overline{T}_L/\overline{T}$, the fraction of lattice kinetic energy and $(1-f)=\overline{T}_p/\overline{T}$, the fraction of plasma kinetic energy. Thus the effective scattering frequency for each mode is a weighted average of the lattice and plasma scattering frequencies in which the weighting is proportional to the relative amount of lattice or plasma energy. It is evident that γ always lies between γ_t and γ_e.

For the longitudinal and $k\to 0$ transverse modes the quantity f is given by

$$f=(\omega^2-\omega_p^2)/(2\omega^2-\omega_p^2-\omega_t^2) \quad , \tag{49}$$

where ω is either ω_A or ω_B. As ω_p increases, f varies from 0 to 1 for the lower modes and from 1 to 0 for the upper modes. Equal mixing occurs at $\omega_p = \omega_t$ where $f = \frac{1}{2}$. f is analogous to the phonon strength S obtained by Varga[2] although not numerically equal to it. In contrast to f, S may be greater than unity for the lower mode at large ω_p.

When a magnetic field is applied, the equality of average kinetic and potential energy densities no longer holds. As a result, γ does not necessarily lie between γ_e and γ_t. For example, the energy of the cyclotron resonance mode in the Faraday configuration is entirely kinetic in nature, the classical orbit of the electron being a circle. In this case $\gamma = 2\gamma_e$. The factor of 2 can be noted in the third factor of the denominator in Eq. (29).

The dependence of the energy distribution of the coupled magnetoplasma–optical-phonon modes is rather complicated. However, the qualitative behavior of two of the modes may be understood by a consideration of the magnetoplasma alone without the lattice. We consider in particular the modes in the Faraday configuration at $k \to 0$. We obtain for the effective scattering frequency

$$\gamma = 2\gamma_e\omega^2/(\omega^2 + \omega_p^2) \quad . \tag{50}$$

In the high field limit, for the right-handed mode $\omega \to \omega_c$ so that $\gamma \to 2\gamma_e$. For the left-handed mode $\omega \to (\omega_p^2/\omega_c)$ so that $\gamma \to 2\gamma_e(\omega_p^2/\omega_c^2)$. The energy of the left-handed mode is largely potential and the energy dissipation is small.

III. EXPERIMENTAL PROCEDURE

The experimental reflectivity curves were obtained using techniques of Fourier transform spectroscopy.[20-22] The apparatus employs a modified Grubb Parsons interferometric spectrometer and is similar to that described by Wheeler and Hill.[23] The radiation from the spectrometer is fed into a brass light pipe and conducted into a liquid-helium Dewar, reflecting off the sample and impinging on the detector, which is a doped semiconducting bolometer. The sample is located at the center of a $2\frac{1}{8}$-in. bore Bitter magnet which provides a maximum field of about 150 kG.

The beam is chopped at the mercury lamp source. The chopped beam is sampled directly by a photocell to provide the reference signal. The detector is biased in series with a load resistor and the output signal is fed into a preamplifier and then into a lock-in amplifier. The dc signal from the lock-in is fed into an integrating digital voltmeter which together with a supplementary unit provides for integration times continuously variable over the range from 10^{-3} to 10^3 sec. During most of the runs a PAR Model CR4A preamplifier was used. However, it was later discovered that a Tektronix Model 122 had a somewhat better signal-to-noise ratio and this unit was employed instead. A PAR Model JB-4 lock-in amplifier and Dymec Model 2401A digital voltmeter were used throughout.

The sampling of the interferogram is controlled by the master control unit, which directs the motion of the movable mirror in a step drive fashion by switching on and off the power to the driving motor. A shaft encoder reads the mirror path difference to the nearest micron. One preset counter is used to set the path increment Δx in multiples of 5 μ. Another counter records the total number of points. On each cycle the mirror is moved to the desired position and stopped. A delay unit with delay time variable from 0 to 15 sec permits the dissipation of the transient developed in the RC filter of the lock-in amplifier before the digital voltmeter begins to integrate. The signal is punched out on paper tape and later converted to cards for processing on an IBM 360 computer.

Mounted on the light pipe is the sample reflectometer which is used for making reflection measurements in the Voigt configuration. The radiation enters the reflectometer through the light pipe from above, goes through a polarizer, reflects in succession off a polished brass mirror, the sample surface, another brass mirror, and then exits through the light pipe below. The sample is a disk 0.360 in. diam by 0.083 in. thick which is held in a removable cap by a retaining ring with the surface parallel to the magnetic field. The paraxial ray is incident upon the sample at an angle of 15°. The nonnormal incidence has an entirely negligible effect on the reflectivity spectrum. The radiation is polarized by a wire-grid polarizer[24,25] which consists of a gold wire grid, vapor deposited on a polyethylene substrate. The polarizer used here is a small disk cut from the commercial item sold by Perkin-Elmer Corp. (PE Part. No. 186-1635). The polarizer may be rotated to vary the polarization and is then secured by a retainer. In order to prevent undesirable scattered radiation from reaching the detector the walls of the reflectometer cavity are coated with 3M Velvet compound.

The detector is an As-doped Ge bolometer of the type described by Wheeler and Hill.[23] The material for the detector element was obtained from Semimetals, Inc. The element is a small chip approximately $0.250 \times 0.200 \times 0.005$ in. thick. Its resistance is about 1 Ω at room temperature and 20 °K at the operating point of 1.3 °K. A stable bath temperature is maintaned by pumping on the liquid helium through a Walker regulator. The actual temperature of the sample itself may be as much as several degrees warmer than 1.3 °K owing to the fact that it is not in direct contact

with the bath.

The chopping frequency was varied over the range 20-100 Hz to determine the best operating point. Although the signal fell off with increasing frequency, the signal-to-noise ratio was apparently rather insensitive to frequency, and an operating frequency of 30 Hz was chosen for convenience.

Three samples of InAs and two of GaSb were used in the present work. All were n-type single crystals. InAs samples 1 and 2 were, respectively, Sn doped and undoped material, having nominal carrier concentrations of 5.5×10^{16} cm^{-3} and 1.8×10^{16} cm^{-3} and mobilities of 2.3×10^{4} cm^2/V sec and 2.4×10^{4} cm^2/V sec. They were obtained from Monsanto. InAs sample 3 was Te doped with a nominal concentration of 2×10^{17} cm^{-3}, supplied by Bell and Howell. GaSb samples 1 and 2 were Te doped with nominal concentrations of 3.7×10^{17} cm^{-3} and 1.2×10^{18} cm^{-3}, respectively, obtained from Alfa Crystals.

The disk-shaped samples were cut ultrasonically from bulk specimens, lapped down to the desirable thickness, polished, and etched to obtain a good optical surface. The InAs samples were etched with a solution of 10% concentrated Br and 90% ethyl alcohol while a solution of 10% HF, 40% HNO_3 and 50% distilled water was used for GaSb. The samples were x rayed to check for damage. The orientation was not determined.

All of the experimental runs were made with a 1/4-mil Mylar beamsplitter in the interferometer. This produced a broadly peaked distribution of spectral energy with a maximum at around 200 cm^{-1} and a usable amount of energy ($\geq$ 20% of maximum) from 40–380 cm^{-1}. Single-sided interferograms were taken with a sampling interval of 10 μ and a maximum path difference of 0.25 cm, giving a spectral resolution of 4 cm^{-1}. Several runs were made with higher resolution but no sharper structure was observed. Reflectivity spectra were obtained by taking ratios of the spectra of the samples to that of a polished brass disk identical in size to the samples. The spectra were calculated from 40–380 cm^{-1} at frequency intervals of 1 cm^{-1}. All runs were made with the electric vector polarized perpendicular to the magnetic field.

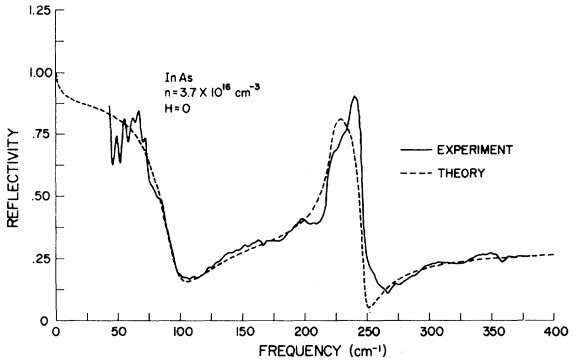

FIG. 4. Reflectivity spectra for InAs sample 1 at $H=0$.

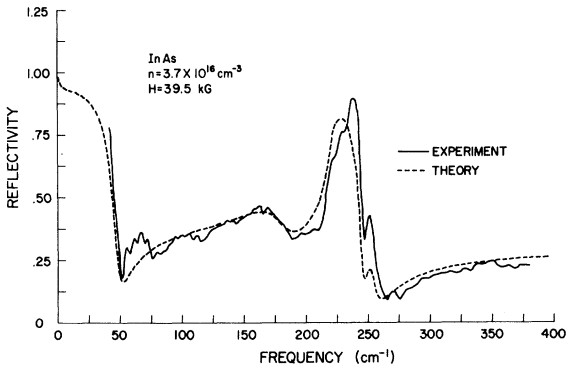

FIG. 5. Reflectivity spectra for InAs sample 1 at H = 39.5 kG.

An integrating time of 10 sec was used on the digital voltmeter. The time constant of the RC filter on the lock-in amplifier was set to 0.3 sec and the delay time to 2 sec. With these settings the runs required slightly over an hour to complete. At zero field signal-to-noise ratios of between 500 and 1000 to 1 were achieved in the interferograms.

IV. EXPERIMENTAL RESULTS AND DISCUSSION

Some typical reflectivity spectra obtained by the techniques described in Sec. III are shown in Figs. 4 and 5. The experimental curves are for sample 1 with a carrier concentration of 3.7×10^{16} cm^{-3}. The accompanying theoretical curves were calculated from the classical model described in Sec. II using the experimentally determined values of the various parameters given in Table I. When the magnetic field is zero (Fig. 4) the main features of the reflectivity curve are the plasmalike edge and a phononlike peak. For this sample the plas-

TABLE I. Summary of results for InAs.

Quantity	Sample 2	Sample 1	Sample 3
n(nominal) (cm^{-3})	1.8×10^{16}	5.5×10^{16}	2×10^{17}
n(expt) (cm^{-3})	1.8×10^{16}	3.7×10^{16}	2.3×10^{17}
ω_t(cm^{-1})	222 ± 3	222 ± 3	222 ± 3
ω_l(cm^{-1})	243 ± 2	243 ± 2	243 ± 2
ω_p(cm^{-1})	74 ± 3	107 ± 3	248 ± 3
γ_t(cm^{-1})	6 ± 2	6 ± 2	6 ± 2
γ_e(cm^{-1})	23 ± 4	26 ± 5	43 ± 8
m^*/m (expt)	0.025 ± 0.001	0.025 ± 0.001	0.028 ± 0.002
m^*_{opt}/m (two-band model)	0.0242	.0250	0.0288
$\mathcal{E}_F$(meV)	10.7	16.9	51.0

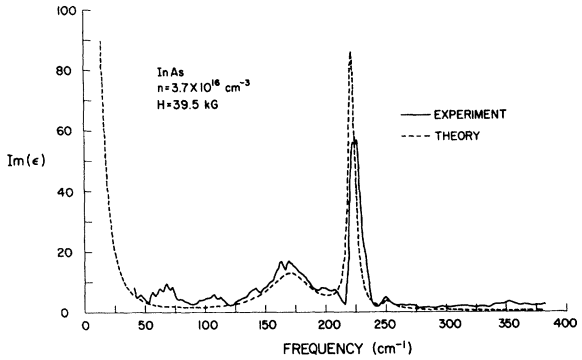

FIG. 6. Im(ϵ) versus frequency for InAs sample 1 at H 39.5 kG.

ma and LO phonon frequencies were determined to be 107 cm^{-1} and 243 cm^{-1}, respectively. The mode repulsion due to plasma–optical-phonon coupling is evident in the downward shift of the plasmalike edge from ω_p. For all samples used in these experiments the scattering frequencies are such that plasmalike features appear much broader than phononlike features.

Figure 5 shows the reflectivity spectrum for a magnetic field of 39.5 kG. The corresponding cyclotron frequency is 147 cm^{-1} for the measured effective mass of 0.025 m. Comparison with Fig. 4 shows that in Fig. 5 the low-frequency plasmalike edge is shifted down in frequency while an additional broad plasmalike peak and higher-frequency sharp phononlike peak also appear.

A computer program was used to calculate the complex reflectance $r(R=|r|^2)$ and subsequently Re(ϵ), Im(ϵ), Re(1/ϵ), and Im(1/ϵ) as a function of frequency from the experimental reflectivity curves by means of the Kramers-Kronig relations. The procedure has been described in the literature[26-28] and will not be discussed here. The output curves were calculated with the same frequency increment and over the same frequency range as the reflectivity curves. The contributions from

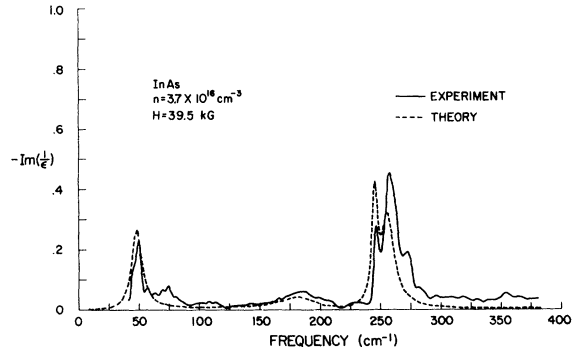

FIG. 7. Im(1/ϵ) versus frequency for InAs sample 1 at H = 39.5 kG.

the unobserved regions of the spectrum were neglected, which is equivalent to the assumption of constant reflectivity in these regions. This assumption is reasonable since the near-infrared and higher-frequency interband transitions contribute negligibly to the far infrared reflectivity.

When Im(ϵ) and Im(1/ϵ) are plotted as a function of frequency, the singularities and zeros of the dielectric function, respectively, are displayed as resonance peaks from which the frequencies and linewidths can be directly measured. Experimental curves of Im(ϵ) and Im(1/ϵ) obtained from the reflectivity spectrum of Fig. 5 are given in Figs. 6 and 7. Corresponding theoretical curves are again shown for comparison. Im(ϵ) (Fig. 6) shows a sharp peak due to the TO phonon, a lower-frequency plasmalike peak and an upper-frequency phononlike peak. Im(1/ϵ)(Fig. 7) has four peaks in all. The upper two are phononlike and the lower two are plasmalike. Note the sharpness of the lowest-frequency peak, indicating the decrease in linewidth with magnetic field.

From the curves of Im(ϵ) and Im(1/ϵ), the frequencies and linewidths of both types of dielectric anomalies were measured as a function of magnetic field. The frequencies were taken to be the positions of the maxima of the peaks and the linewidths to be the full widths at half-maximum. The peaks were hand smoothed when necessary to eliminate noise. On occasion, one side of a peak was obscured by additional features. (Note, for example, the structure on the high-frequency side

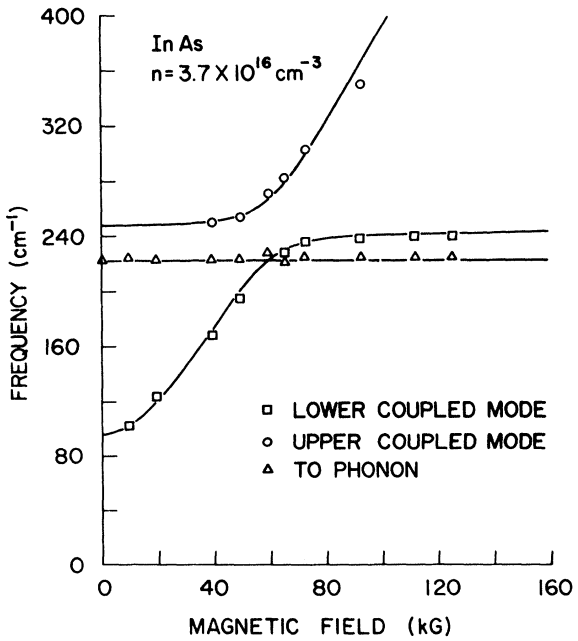

FIG. 8. Frequencies of the singularities of ϵ versus magnetic field for InAs sample 1.

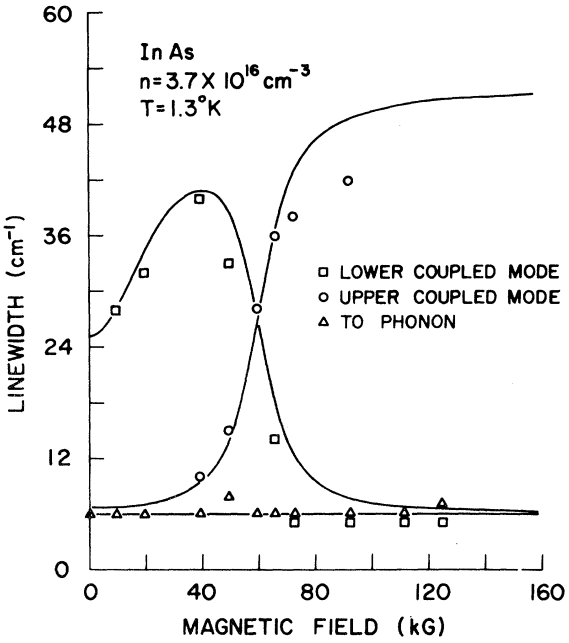

FIG. 9. Linewidths of the singularities of ϵ versus magnetic field for InAs sample 1.

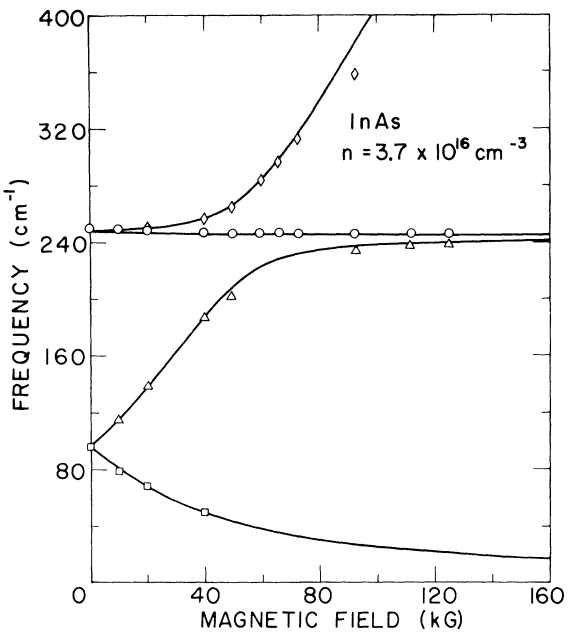

FIG. 10. Frequencies of the zeros of ϵ versus magnetic field for InAs sample 1.

of the upper peak in Fig. 7.) In this case, the linewidth was taken to be twice the half-width of the clear side of the peak.

The experimental values of the frequencies and linewidths of the dielectric anomalies are plotted as a function of magnetic field for sample 1 in Figs. 8–11. Theoretical curves calculated from the expressions derived in Sec. II using the parameters of Table I, are also shown. Figure 8 shows the frequencies of the singularities of ϵ. The TO phonon is unaffected by the field, having the frequency ω_t. The other two singularities interact and exhibit mode repulsion. The lower one is plasmalike at low field and becomes LO phononlike at high field; correspondingly, the upper one is LO phononlike at low field and plasmalike at high field. The change in character of the singularities with magnetic field is even more strikingly illustrated by the linewidths (Fig. 9). Again the TO phonon is seen to be independent of the field. The linewidth of the upper singularity begins at a low value and increases to a value considerably greater than the electron scattering frequency γ_e (26 cm^{-1}) at high field. [In theory, it should approach 2 γ_e as the mode becomes more like cyclotron resonance in nature (see Sec. II).] The linewidth of the lower singularity first increases as some cyclotron-resonance character is introduced by the field and then decreases to a low value as it becomes LO phononlike.

The frequencies and linewidths of the zeros of ϵ are shown in Figs. 10 and 11. Two of the zeros, i.e., the second and fourth in order of increasing frequency, behave in a fashion similar to the two interacting singularities. The third zero is LO phononlike over the entire field range and the frequency and linewidth show little change with field. The lowest-frequency zero shows a decrease in

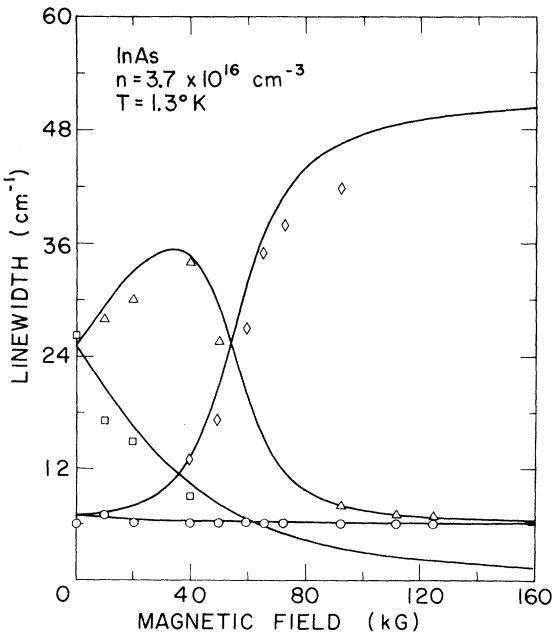

FIG. 11. Linewidths of the zeros of ϵ versus magnetic field for InAs sample 1. Symbols correspond to those of Fig. 10.

both frequency and linewidth with field as discussed in Sec. II.

Similar comparisons of the experimental and theoretical magnetic field dependence of the frequencies and linewidths were made for samples 2 and 3. The qualitative behavior was found to be the same as for sample 1. For sample 2 with the lowest carrier concentration the coupling and mode repulsion were weak. The transition in the character of the modes from phononlike to plasmalike was quite abrupt. As the concentration increased, the coupling and mode repulsion became stronger and the transition more gradual.

The experimental results for the three samples are summarized in Table I. All of the constants were determined experimentally except for ϵ_∞. ϵ_∞ could not be determined directly from experiment with good accuracy and a previously measured value[29] of 11.6 was used. The following analysis procedure was followed:

(a) ω_l was calculated using the measured values of ω_2 and ω_3 at the highest magnetic field used and the following approximate relation valid in the high field limit

$$\omega_l \approx \tfrac{1}{2}(\omega_2+\omega_3) . \tag{51}$$

(b) ω_t was measured directly at zero field. However, because the measured value of ω_t was found to be very sensitive to the sources of experimental error, the final value used was chosen such that ω_t and the values of ω_A and ω_B calculated from the least-squares fit in (c) all agreed with the measured values to within the estimated experimental error. (c) Given ω_l and ω_t, ω_p was adjusted to achieve a least-squares fit of the calculated values of ω_A and ω_B with their measured values at zero field. (d) Given ω_l, ω_t, and ω_p, theoretical curves of the frequencies of both the singularities and zeros of ϵ were calculated for various values of m^*. These were compared with the experimental plots and m^* chosen to achieve the best fit with the data. (e) n was calculated from the relation $\omega_p^2 = (4\pi ne^2/m^*\epsilon_\infty)$. (f) γ_t was measured directly at zero field. (g) γ_e was calculated from Eq. (31) using the values of γ_A and γ_B measured at zero field.

The values of ω_t and ω_l determined here are consistent with those reported by Hass and Henvis.[30]

The experimental error arises mainly from uncertainty in absolute intensity of the reflectivity and from noise. In the middle of the spectral range the uncertainty in absolute intensity is estimated to be ± 10% and the noise is a few percent. Both quantities increase significantly at the ends of the spectral range due to the falloff of energy in the beam.

In order to determine the effect of the uncertainty in absolute intensity on the experimental results, a typical reflectivity curve was artificially modified by (i) multiplying the entire curve by a constant factor, and (ii) changing the value of R_∞, the asymptotic value of R at high frequency, and run through the Kramers-Kronig analysis program. The intensities of the peaks in $\mathrm{Im}(\epsilon)$ and $\mathrm{Im}(1/\epsilon)$ were found to be considerably more sensitive to these modifications than were the frequencies and linewidths. The TO phonon peak was the most sensitive of all. It was also discovered that when the value of R_∞ was increased beyond a certain point, negative values appeared in $\mathrm{Im}(\epsilon)$. Anomalously high or low values of R_∞ were actually observed in some experimental reflectivity curves, the former giving rise to negative values of $\mathrm{Im}(\epsilon)$.[16] These curves were later modified to make R_∞ equal to its theoretical value and were then rerun through the Kramers-Kronig analysis program.

The experimental errors are estimated to be as follows: The error in frequency varies from ± 2 cm^{-1} for the sharpest phononlike peaks to ± 5 cm^{-1} for the broadest plasmalike peaks. The error in linewidth is ± 20% while the error in intensity is ± 50%. ω_t and γ_t are expected to be somewhat more imprecise than the frequencies and linewidths of the other phononlike modes, the estimated errors being ± 3 cm^{-1} and ± 2 cm^{-1}, respectively.

In general, there is good agreement between the experimental curves of reflectivity, $\mathrm{Im}(\epsilon)$ and $\mathrm{Im}(1/\epsilon)$, and the theoretical curves calculated from the model as seen in Figs. 1–4. Better agreement is achieved for the frequencies and linewidths of the peaks in $\mathrm{Im}(\epsilon)$ and $\mathrm{Im}(1/\epsilon)$ than for the intensities, as is expected from the foregoing error analysis. However, a few discrepancies between theory and experiment may be noted. Additional structure appears in the experimental curves at low frequencies. This structure is noise which appears because of the low signal-to-noise ratio in this region as mentioned above. Additional structure also appears in the reflectivity curves directly above the TO phonon and LO phononlike reflection edges, showing up in the curves of $\mathrm{Im}(\epsilon)$ and $\mathrm{Im}(1/\epsilon)$ as a broadening of the peaks on the high-frequency side. The LO phononlike peak is broadened considerably and several subsidiary peaks are present. This structure was observed for all three samples and did not show any systematic change with magnetic field. Its origin is not understood at present, but it might be the result of surface effects. The modification of reflectivity spectra by surface effects has been observed previously.[31]

To within experimental error, there is general agreement between the experimental and theoretical dependence of the frequencies and linewidths of the dielectric anomalies on magnetic field.

There is one significant deviation. At high magnetic fields (≈ 90 kG) in the frequency curves for sample 1 the experimental frequency of the highest-frequency mode is lower than the theoretical value. A similar deviation was noted in the curves of sample 2. This deviation is thought to result from the increase of effective mass with magnetic field as discussed below.

In our analysis so far we have considered the electron effective mass m^* to be an adjustable parameter independent of magnetic field. Due to the nonparabolic dependence of the energy of the conduction band on wave vector, which arises from the interaction between the conduction band and other energy bands, m^* is a function of both carrier concentration and magnetic field. We now proceed to calculate this dependence using the two-band model,[32-34] which assumes only two sets of interacting bands, in this case the conduction and valence bands.

For an isotropic band, which is the case for the conduction band of InAs and most III–V compounds, the two-band model yields the following simple relation of energy to wave vector:

$$\mathcal{E} = -\tfrac{1}{2}\mathcal{E}_g + [\tfrac{1}{2}\mathcal{E}_g + (\hbar^2 k^2/2m_0^*)\mathcal{E}_g]^{1/2} \quad . \tag{52}$$

Here, $\mathcal{E}_g$ is the energy gap, m_0^* the effective mass at the bottom of the band, and $\mathcal{E}$ is measured from the bottom of the band.

When the energy dependence of the band is nonparabolic, the effective mass may be defined in several ways.[35] The mass appearing in the expression for the plasma frequency ω_p is the optical effective mass $m_{\rm opt}^*$ which characterizes incremental fluctuations of the electron plasma about equilibrium. For a degenerate plasma $m_{\rm opt}^*$ is related to the derivative of energy with respect to wave vector at the Fermi energy $\mathcal{E}_F$. In the isotropic case the relation is[36]

$$m_{\rm opt}^* = \frac{\hbar^2 k}{d\mathcal{E}/dK}\Big|_{\mathcal{E}=\mathcal{E}_F} \quad . \tag{53}$$

For the two-band model $m_{\rm opt}^*$ is found to increase in a linear fashion with $\mathcal{E}_F$

$$m_{\rm opt}^* = m_0^*[1 + (2\mathcal{E}_F/\mathcal{E}_g)] \quad . \tag{54}$$

Table I gives $m_{\rm opt}^*$ and $\mathcal{E}_F$ for the three samples of InAs calculated from (53) using the values of n derived from experiment and taking $\mathcal{E}_g = 0.41$ eV[37] and $m_0^* = 0.023$.[38]

When a magnetic field H is applied along the z direction, the energies of the conduction-band Landau levels are given in the two-band model by

$$\mathcal{E}_l \pm = -\tfrac{1}{2}\mathcal{E}g + \{(\tfrac{1}{2}\mathcal{E}g)^2 + [(l+\tfrac{1}{2})\hbar\omega_c + (\hbar^2 k_z^2/2m_0^*) \pm \tfrac{1}{2}\beta g_0 H]\mathcal{E}g\}^{1/2}, \tag{55}$$

where l is the Landau quantum number, β the Bohr magneton, g_0 the effective g factor at the bottom of the band, and $\omega_c = (eH/m_0^* c)$.

In the magnetic case the expression for $m_{\rm opt}^*$ involves only the derivative with respect to k_z of the energy and is found to be given by Eq. (54) just as in the zero-field case. Thus, the only dependence of $m_{\rm opt}^*$ on magnetic field is through $\mathcal{E}_F$. The effective mass appearing in ω_c is the cyclotron resonance effective mass $m_{\rm cr}^*$ which characterizes an optical transition between two sucessive Landau levels. In the classical limit ($\hbar\omega_c \ll \mathcal{E}_F$) $m_{\rm cr}^*$ and $m_{\rm opt}^*$ are equal but as the field increases $m_{\rm cr}^*$ may differ considerably from $m_{\rm opt}^*$ because the energies involved in the cyclotron-resonance transition may depart appreciably from the Fermi level. In the quantum limit ($\hbar\omega_c > \mathcal{E}_F$), when only the lowest transition is possible, $m_{\rm cr}^*$ is given by the approximate relation

$$m_{\rm cr}^* \approx m_0^*[1 + (4\hbar\omega_c/\mathcal{E}g)]^{1/2} \quad . \tag{56}$$

The effect of nonparabolicity may be included in a phenomenological manner in the theroy of Sec. II by calculating $m_{\rm opt}^*$ and $m_{\rm cr}^*$ as a function of magnetic field and using them in the expressions for ω_p and ω_c, respectively. This procedure should result in a better fit to the data. Here we shall confine ourselves to a discussion of the low-field and high-field regimes.

As stated above, the experimental value of m^* was obtained by fitting the theoretical curves of frequency versus magnetic field to the data. The value of m^* so obtained should be close to $m_{\rm opt}^*$ since it is a low field that the frequencies of the observable plasmalike modes are most sensitive to a variation in m^*. Table I shows that the experimental value of m^* agrees very well with the value of $m_{\rm opt}^*$ calculated from Eq. (54) for all three samples.

The approximate value of the magnetic field where the transition to the quantum limit occurs may be calculated from the parameters of Table I for the three samples. This field is found to be 22 kG for sample 2, 35 kG for sample 1, and 119 kG for sample 3. Thus, for both samples 1 and 2 the field of about 90 kG at which significant deviations in the frequency of the upper modes are observed is well into the quantum limit. Equation (56) should be valid for $m_{\rm cr}^*$ over the value of 0.025 used in the theoretical curves for both samples. Since the frequency of the upper modes at this field is largely dominated by ω_c, the increase in $m_{\rm cr}^*$ should result in a reduction of about 30 cm^{-1} in frequency. The observed shift is of this magnitude.

The plasma loss, which is taken into account phenomenologically by the electron scattering frequency γ_e, is dominated by single-particle scat-

tering of electrons off ionized impurity atoms. As seen in Table I the value of γ_e determined from experiment is observed to increase with carrier concentration. Following Conwell and Weisskopf[39] we may calculate a simple expression for the dependence of electron scattering on carrier concentration under the assumption that the electrons undergo Rutherford scattering by the Coulomb potential of the impurity atoms. If we take the electron plasma to be degenerate and assume that each impurity atom dominates the scattering within a sphere of radius $d(=\frac{1}{2}n^{-1/3})$, the electron scattering frequency is found to be

$$\gamma_e = 2v_F n^{1/3}[\ln(1+x^2)]/x^2 \ , \qquad (57)$$

where $x=\epsilon_\infty dm^* v_F^2/e^2$, v_F being the Fermi velocity.

In Fig. 12, the experimental values of γ_e for the three samples are plotted as a function of n and compared with a theoretical curve calculated from Eq. (57) using a constant effective mass $m^* = 0.025$ m. The corrections to the curve arising from the variation in m^* with n are estimated to be small. Good agreement is obtained between theory and experiment. Note that at high concentration γ_e increases as $\ln(n)$ rather than directly as n. As n increases, the Fermi velocity of the electrons increases so that the effect of the scattering from each impurity atom is diminished.

Experiments were also carried out with two samples of GaSb. The carrier concentrations were approximately equal so that the results did not differ appreciably. The best results were obtained with sample 2 which had a carrier concentration 4.1×10^{17} cm^{-3}. The behavior of the modes was found to be qualitatively the same for InAs, the main difference being that because of the heavier effective mass in GaSb the frequencies changed more gradually with field. The following values were obtained for the various parameters: $\omega_t = 231\pm3$ cm^{-1}, $\omega_l = 240\pm2$ cm^{-1}, $\omega_p = 235\pm4$ cm^{-1}, and $m^* = 0.044\pm0.003$. The values of ω_t, ω_l, and m^*[40,41] are consistent with previous measurements. ϵ_∞ was taken to be 15.2.[29]

A complete analysis of the linewidths was not carried out, owing to the fact that the linewidths of the plasmalike peaks were rather broad and hard to estimate. The TO phonon linewidth appeared to be less than the resolution width of 4 cm^{-1}, indicating that a complete study of linewidths should employ better resolution.

V. CONCLUSIONS

These experiments have shown that the experimental behavior of the frequencies and linewidths of the coupled magnetoplasma–optical-phonon modes in n-type InAs is in agreement with the predictions of the classical theory of long-wavelength optical vibrations in crystals, based on the equations of motion for lattice ions and electrons. The observed increase in electron effective mass with carrier concentration due to the nonparabolicity of the conduction band is in accordance with that predicted by the two-band model. Discrepancies between theory and experiment seen in the curves of mode frequency versus magnetic field at high fields can be accounted for by the increase in effective mass with magnetic field also predicted by the two-band model. At low temperatures the observed plasma loss can be accounted for quite well by a Rutherford scattering model for single-particle scattering by ionized impurities in a degenerate electron gas. The observed behavior of the mode frequencies in n-type GaSb is also in accordance with theory.

This work has also demonstrated that reflectivity measurements combined with the Kramers-Kronig-analysis procedure are an excellent technique for the study of the far-infrared properties of semiconductors. Some improvements and additions could be made to the present system. The noise could be reduced by improved detectors. Very careful alignment of the sample and standardization of the absolute signal intensity for each set

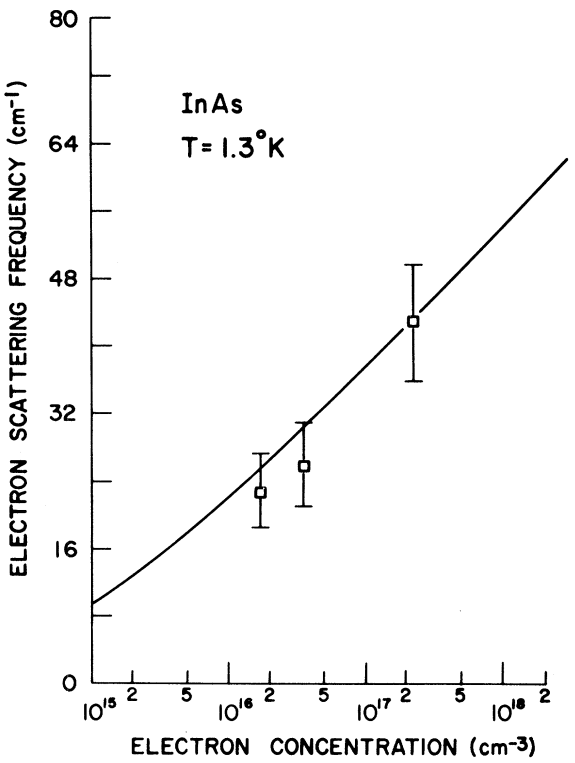

FIG. 12. Dependence of electron scattering frequency on carrier concentration for the three samples. Theoretical curve is calculated from Eq. (57).

of runs could probably reduce the uncertainty in the value of the reflectivity to a few percent. These two improvements would result in increased accuracy of the frequency and linewidth measurements. It would also be of value to have the detector and the sample cooled separately so that the sample termperature could be varied independently for temperature-dependent studies.

This work could be extended by experiments in both InAs and other materials. A quantitative study of the effect of the nonparabolicity of the conduction band on the behavior of the coupled magnetoplasma–optical-phonon modes would be very valuable. Experiments should be done at many different values of magnetic field to observe the structure in the curves of frequency and linewidth versus magnetic field due to the quantum effects. To observe clearly the highest-frequency modes at maximum field, the spectral range of the apparatus should be increased to include frequencies up to about 600 cm^{-1}.

It would also be of considerable interest to study the temperature dependence of the effective linewidths to test the validity of the theory over a wide range of temperatures. Both the electron and lattice scattering frequencies should change significantly between liquid-helium temperature and room temperature. For most materials a resolution better than the 4 cm^{-1} employed in the present work would be advisable, owing to the sharpness of the phonon peaks.

Studies of the coupled magnetoplasma–optical-phonon modes by Raman-scattering techniques would compliment optical-reflectivity measurements. Variation of the angle between incident and scattered radiation would permit a determination of the frequencies, linewidths, and intensities of the modes as a function of wave vector. Thus, the dispersion of the modes could be measured directly. Such a procedure has been used by Henry and Hopfield[42] to study the polariton dispersion in GaP.

On the theoretical side, the full many-body quantum theory of magnetoplasma–optical-phonon coupling which has been recently developed by Rabitz and Lax[6] should be extended to include linewidth calculations to compare with classical theory and experiment. The linewidth would require higher-order terms such as deformation coupling of electrons to acoustical modes and anharmonic multiphonon coupling between optical phonons and acoustical phonons.

ACKNOWLEDGMENTS

The authors would like to thank K. J. Button for his interest in this work and for his help in obtaining samples. They are most grateful to J. Christensen for his tireless efforts in the construction and maintenance of the apparatus. They would also like to thank Professor R. G. Wheeler for his many valuable suggestions on the design of the experimental system and experimental techniques, L. G. Rubin and R. Arndt for their assistance with the electronic system, J. Alexander and Catherine Beaton for sample preparation, and J. Parrish for the Kramers-Kronig-analysis computer program.

---

*Present address: General Electric Company, Cleveland, Ohio.

†Also, Physics Department, Massachusetts Institute of Technology, Cambridge, Mass. 02139.

‡Supported by the U.S. Air Force Office of Scientific Research.

[1]I. Yokota, J. Phys. Soc. Japan 16, 2075 (1961).

[2]B. B. Varga, Phys. Rev. 137, A1896 (1965).

[3]K. S. Singwi and M. P. Tosi, Phys. Rev. 147, 658 (1966).

[4]I. Yokota, J. Phys. Soc. Japan Suppl. 21, 738 (1966).

[5]M. P. Greene, A. Houghton, and J. J. Quinn, Phys. Letters 20, 238 (1966).

[6]R. Rabitz and B. Lax (unpublished).

[7]S. Iwasa, Y. Sawada, E. Burstein, and E. D. Palik, J. Phys. Soc. Japan Suppl. 21, 742 (1966).

[8]R. Kaplan, E. D. Palik, R. F. Wallis, S. Iwasa, E. Burstein, and Y. Sawada, Phys. Rev. Letters 18, 159 (1967).

[9]A. Mooradian and G. B. Wright, Phys. Rev. Letters 16, 999 (1966).

[10]R. A. Cowley and G. Dolling, Phys. Rev. Letters 14, 549 (1965).

[11]S. G. Bishop, Bull. Am. Phys. Soc. 13, 430 (1968).

[12]S. G. Bishop and B. W. Henvis, Solid State Commun. 7, 437 (1969).

[13]P. R. Wallace, Can. J. Phys. 43, 2162 (1965).

[14]P. R. Wallace, Can. J. Phys. 44, 2495 (1966).

[15]R. W. Stimets, Bull. Am. Phys. Soc. 13, 752 (1968).

[16]R. W. Stimets and B. Lax, Phys. Letters 28A, 321 (1968).

[17]G. B. Wright and B. Lax, J. Appl. Phys. 32, 2113 (1961).

[18]M. Born and K. Huang, *Dynamical Theory of Crystal Lattices* (Oxford U. P., Oxford, England, 1954), pp. 82–100.

[19]See Ref. 18, pp. 100-116.

[20]J. Connes, Rev. Opt. 40, 45 (1961); 40, 116 (1961); 40, 171 (1961); 40, 231 (1961).

[21]J. Strong and G. A. Vanasse, J. Opt. Soc. Am. 49, 844 (1959).

[22]P. L. Richards, J. Opt. Soc. Am. 54, 1474 (1964).

[23]R. G. Wheeler and J. C. Hill, J. Opt. Soc. Am. 56, 657 (1966).
[24]G. R. Bird and M. Parrish, J. Opt. Soc. Am. 50, 886 (1960).
[25]M. Hass and M. O'Hara, Appl. Opt. 4, 1027 (1965).
[26]T. S. Robinson, Proc. Phys. Soc. (London) B65, 910 (1952).
[27]G. Andermann, A. Coron, and D. A. Dows, J. Opt. Soc. Am. 55, 1210 (1965).
[28]D. W. Berreman, Appl. Opt. 6, 1519 (1967).
[29]O. Madelung, *Physics of III–V Compounds* (Wiley, New York, 1964), p. 101.
[30]M. Hass and B. W. Henvis, J. Phys. Chem. Solids 23, 1099 (1962).
[31]D. Kleinman and W. G. Spitzer, Phys. Rev. 118, 110 (1960).
[32]B. Lax, Bull. Am. Phys. Soc. 5, 167 (1960).
[33]B. Lax and J. G. Mavroides, in *Advances in Solid-State Physics*, edited by F. Seitz and D. Turnbull (Academic, New York, 1960), Vol. II.
[34]B. Lax, J. G. Mavroides, H. J. Zeiger, and R. J. Keyes, Phys. Rev. Letters 5, 241 (1960).
[35]See Ref. 29, p. 35.
[36]See Ref. 29, p. 81.
[37]F. Matossi and F. Stern, Phys. Rev. 111, 472 (1958).
[38]E. D. Palik and R. F. Wallis, Phys. Rev. 123, 131 (1961).
[39]E. Conwell and V. F. Weisskopf, Phys. Rev. 77, 388 (1950).
[40]H. Piller, J. Phys. Chem. Solids 24, 425 (1963).
[41]H. Piller and V. A. Patton, Phys. Rev. 129, 1169 (1963).
[42]C. H. Henry and J. J. Hopfield, Phys. Rev. Letters 15, 964 (1965).

PHYSICAL REVIEW B VOLUME 1, NUMBER 12 15 JUNE 1970

Effects of Co^{60} Gamma Irradiation on Epitaxial GaAs Laser Diodes*

C. E. Barnes
Sandia Laboratories, Albuquerque, New Mexico 87115
(Received 22 December 1969)

The characteristics of defects introduced in epitaxial GaAs by room-temperature Co^{60} irradiation have been studied by observing the degradation of light emission from GaAs laser diodes. The luminescence degradation is indicative of a decrease in electron lifetime in the p-type region brought about by the introduction of nonradiative recombination centers. These defects anneal in a single stage centered at 237 °C. Isothermal-annealing studies show that the defects anneal by a first-order kinetic process with an activation energy of 1.7 eV and a preexponential factor of 10^{13} sec^{-1}. The annealing properties of the defect suggest that it is a complex whose dissociation is the limiting step in the recovery process. The defects can also anneal at temperatures as low as 76 °K under the influence of a strong forward bias. A dc forward bias at 2.2×10^{2} A/cm^2 at room temperature for 1 h produces complete recovery of the light intensity. The possibility of annealing due to heating while under strong forward bias has been considered and does not appear to be responsible for the bias annealing. Rather, the forward-bias-induced recovery is thought to be due to an increase in the probability of annihilation because of a change in charge state of the defect complex following capture of a minority carrier. The various aspects of forward-bias annealing observed in this study can be explained by this model. On the basis of the above results, the complex has been tentatively identified as consisting of an impurity and an As interstitial.

INTRODUCTION

The luminescence emitted from GaAs because of various forms of excitation has been the subject of intensive study during recent years. The effects of radiation on GaAs luminescence have received less attention. With the exception of a few papers on photoluminescence and cathodoluminescence,[1-5] radiation effects investigations have concentrated on electroluminescence, especially in light-emitting diodes.[6] Aukerman and co-workers have extensively studied electron-irradiated GaAs diodes.[7-10] The primary aim of these latter investigations was to use radiation as a tool for discovering the mode of operation of light-emitting diodes. For example, it was shown that the electroluminescence can be due to either recombination of electrons injected into the p-type side of the diode or recombination in the depletion region according to a "band-filling" model. The predominance of either type of recombination depends on such parameters as doping level, temperature, and forward-bias voltage. In other studies, Saji and Inuishi[11] have shown that Co^{60} irradiation increases the threshold current of laser diodes at 77 °K, while Petree[12] found a degradation threshold for neutron